A 3D low-order panel method for unsteady aerodynamic problems

E. Ortega
R. Flores
E. Oñate

Publication CIMNE Nº-343, May 2010

A 3D low-order panel method for unsteady aerodynamic problems

E. Ortega
R. Flores
E. Oñate

Publication CIMNE Nº-343, May 2010

International Center for Numerical Methods in Engineering
Gran Capitán s/n, 08034 Barcelona, Spain

A 3D LOW-ORDER PANEL METHOD FOR UNSTEADY AERODYNAMIC PROBLEMS

Enrique Ortega, Roberto Flores and Eugenio Oñate

International Center for Numerical Methods in Engineering (CIMNE)
Universidad Politécnica de Cataluña
Edificio C1, Campus Norte, UPC
Gran Capitán, s/n, 08034 Barcelona, España

Abstract. An unsteady low-order panel method for three-dimensional subsonic analyses is presented. The method, which is based on well-established techniques in computational aerodynamics, is intended to achieve a cost-effective solution of unsteady flows around arbitrary aerodynamic configurations. This work has two main objectives. First, to relax geometry discretization requirements and, second, to simplify the treatment of problems in which the analysis configuration moves along specified flight paths and/or changes its geometry during the simulation. Following this aim, a time-marching solution procedure is adopted in conjunction with a free-wake model which avoids iterative solutions for wake shape and position. The suitability of the present approach for solving typical aerodynamic problems is illustrated by means of several numerical examples.

1. INTRODUCTION

The behaviour of general fluid flows is described by the Navier-Stokes system of equations. In particular problems, these equations allow introducing simplifications intended to achieve reduced equation models, easier to analyze and solve with a lesser computational cost. In the study of high-Reynolds number flows around aerodynamic bodies, the analysis domain can be divided into a zone where the viscous and rotational effects of the fluid are relevant and a zone where they can be neglected. According to Prandtl's boundary layer concept, the zone where viscous effects are important is confined to thin boundary layers developed close to the body and thin wake regions. The rest of the fluid field can be considered to be inviscid and irrotational. This ideal flow field outside the viscous regions can be mathematically described by a Laplace's equation for a scalar field named *velocity potential* and its solution allows determining many features of aerodynamic attached flows with considerably accuracy. It should be noticed that the viscous effects of the flow must be negligible for the solution of the potential problem to render an accurate representation of the flow phenomena. Fortunately, this assumption is valid for a large range of typical problems in aerodynamics.

The solution of potential problems has been extensively addressed in aerodynamics since the beginning of the past century. Most advanced techniques developed for potential aerodynamics problems are based on Green's second identity and take advantage of the fact that the velocity potential field is linear. Hence, simple harmonic flow functions (singularities) subject to suitable boundary conditions can be combined and distributed along the body under study in order to construct more complex flow fields. Numerical models based on this approach are known as *panel methods*. These techniques are extremely advantageous because any flowfield of interest can be resolved by distributing singular functions over the body boundaries without the need of defining and solving a grid for the surrounding fluid domain. Thus, the computational effort is drastically reduced with respect to standard volume-based methods (e.g. Finite Differences, Finite Volumes and Finite Elements) at the same time that pretty accurate solutions can be achieved. This explains why panel methods, though based on a rather old technology, are still a primary simulation tool widely used for aerodynamic analysis and design. A comprehensive description of the most typical panel methods is presented by Katz and Plotkin in [1]. Furthermore, a wide variety of applications of panel methods can be found in the literature; see for instance the treatment of unsteady subsonic problems in [2], transonic and supersonic flows in [3, 4] and coupled inviscid-boundary layer analyses in [5].

In this work we present a numerical model based on a three-dimensional low-order panel technique which is intended to perform subsonic unsteady analyses of arbitrary aerodynamic configurations. The methodology employed follows the lines proposed in [2, 6] and addresses important issues such as a simpler geometry discretization, the treatment of bodies which move or deform in time during the simulation and a straightforward wake definition. In the following, Section 2 reviews the main features of the potential flow model. The panel technique applied for its solution is described in Section 3 and details concerning the numerical implementation are given in Sections 4 and 5. Three numerical test cases are presented in Section 6 in order to assess the performance of the method. Finally, some conclusions of the work and future lines of investigation are outlined in Section 7.

2. THE POTENTIAL FLOW MODEL

The potential flow model describes the physics of inviscid and irrotational flows. Under these assumptions, the incompressible fluid equations reduce to

$$\nabla \times \mathbf{V} = 0 \tag{1}$$

$$\nabla \cdot \mathbf{V} = 0 \tag{2}$$

where Eq. (1) models the dynamics of an irrotational fluid and Eq. (2) ensures mass conservation. Due to the fact that the curl of a gradient is identically equal to zero, the irrotational condition given by Eq. (1) can be fulfilled by defining the velocity field as

$$\mathbf{V} = \nabla \Phi \tag{3}$$

being $\Phi = \Phi(X,Y,Z)$ a scalar function known as *velocity potential*. Then, replacing Eq. (3) into Eq. (2), a Laplace's problem for the velocity potential is obtained

$$\nabla^2 \Phi = 0 \tag{4}$$

which must be solved with suitable boundary conditions according to the problem under consideration. For aerodynamic analyses, typical conditions are:

a. Far-field condition: the flow disturbances must disappear far away from the body.

b. Neumann condition: the normal component of the velocities across the body's boundary must be equal to zero if the boundary is solid, or equal to a prescribed value when flow across the boundary is allowed (transpiration conditions).

In conjunction with boundary conditions (a) and (b), Eq. (4) leads to a mathematically well-posed problem. However, its solution is not uniquely determined unless the circulation around the body is fixed (see a mathematical proof in [1]). The correct amount of circulation to be specified is determined on physical grounds by the Kutta condition. The latter leads to ideal flow solutions in agreement with the real attached flow behaviour and can be enunciated as:

c. The circulation around the body is fixed in such a way that the resulting velocity at the trailing edge is finite and continuous, i.e. the flow leaves the body smoothly.

When conditions (a)-(c) are applied, the potential problem is completely defined and the solution of the flow field around a lifting aerodynamic body proceeds as follows. The velocity potential is solved from Eq. (4) (or some equivalent form) and the velocity field is computed from Eq. (3). Thus, the pressures acting on the body can be obtained by applying the Bernoulli's equation, which results from integrating the momentum conservation equations in an inviscid and irrotational flow. Finally, the aerodynamic forces, the main objective of any aerodynamic analysis, can be readily calculated by integrating the pressure distribution over the body boundaries.

Notice that no temporal terms are involved in Eqs. (4) and (3) when solved for the velocity field. This can be explained by the fact that in the incompressible limit, the speed of the sound goes to infinite causing the flow field to adapt instantaneously to changes in the boundary conditions. As a result, time-dependence in the problem solution can be introduced by defining unsteady boundary conditions.

2.1 Coordinate systems for unsteady analyses

A body-fixed coordinate system (x,y,z) and a steady inertial frame (X,Y,Z) are defined in order to facilitate the treatment of unsteady problems. The body system is attached to a reference point in the analysis configuration and follows the motion of the latter in the steady inertial frame. At time $t = 0$ both coordinates systems are coincident and at rest. Then, at time $t > 0$, the position and orientation of the body system is determined by the translation of its origin $\mathbf{R}_0(t) = \left(\mathrm{X}_0, \mathrm{Y}_0, \mathrm{Z}_0\right)$ in the inertial frame and the Euler rotation angles $\boldsymbol{\Theta}(t) = (\phi, \theta, \Psi)$ around the fixed axes. As both $\mathbf{R}_0(t)$ and $\boldsymbol{\Theta}(t)$ are considered to come from a specified flight path data, the velocity of the body system's origin $\mathbf{V}_0 = \left(\dot{\mathrm{X}}_0, \dot{\mathrm{Y}}_0, \dot{\mathrm{Z}}_0\right)$ and the rates of rotation $\boldsymbol{\omega} = (\dot{\phi}, \dot{\theta}, \dot{\Psi})$ can be obtained. Then, the instantaneous kinematic velocity at each point on the body can be evaluated in the inertial axes according to

$$\mathbf{v} = \mathbf{V}_0 + \boldsymbol{\omega} \times \boldsymbol{r} + \mathbf{v}_{rel} \tag{5}$$

where $\boldsymbol{r} = (x, y, z)$ is the position vector of a given point with respect to the body's origin and $\mathbf{v}_{rel} = \left(\dot{\mathrm{x}}, \dot{\mathrm{y}}, \dot{\mathrm{z}}\right)$ is a relative velocity accounting for deformations of the body.

2.2 The Neumann boundary condition

In potential flow problems, the Neumann condition (b) prescribes the normal component of the velocity across the boundaries. In the body axes this condition results

$$\left(\nabla\Phi - \mathbf{v}\right) \cdot \hat{\boldsymbol{n}} = \mathrm{V_N} \tag{6}$$

where $\nabla\Phi$ is the total velocity of a fluid particle, $\mathbf{v}$ is the kinematic local velocity of the boundary (Eq. (5)), $\hat{\boldsymbol{n}}\left(x, y, z\right)$ is the outward normal vector to the boundary and $\mathrm{V_N}$ is a specified normal velocity (relative to the boundary) aimed at modeling transpiration surfaces. Note that the boundary condition (6) changes in time as a consequence of the body motion in the stationary frame and introduces time dependence in the potential problem solution.

3. UNSTEADY LOW-ORDER PANEL METHOD

The aerodynamic problem to be solved consists of a three-dimensional body immerse in an ideal fluid flow Ω which is enclosed by a far-field boundary S_∞. The body is defined by the boundary S_B, with normal vector $\hat{\boldsymbol{n}}$ pointing outside the analysis domain Ω. S_W represents the upper (U) and lower (L) sides of a thin wake which extends downstream from the body introducing a discontinuity in the velocity potential field. As observed in Figure 1, the boundaries $S = S_B + S_W$ divide the problem domain into external and internal regions. The external region contains the flowfield of interest, defined by a velocity potential Φ. In the internal region, a fictitious flow is assumed due to a velocity potential Φ_i. The velocity potentials Φ and Φ_i are considered to be harmonic functions satisfying Eq. (4).

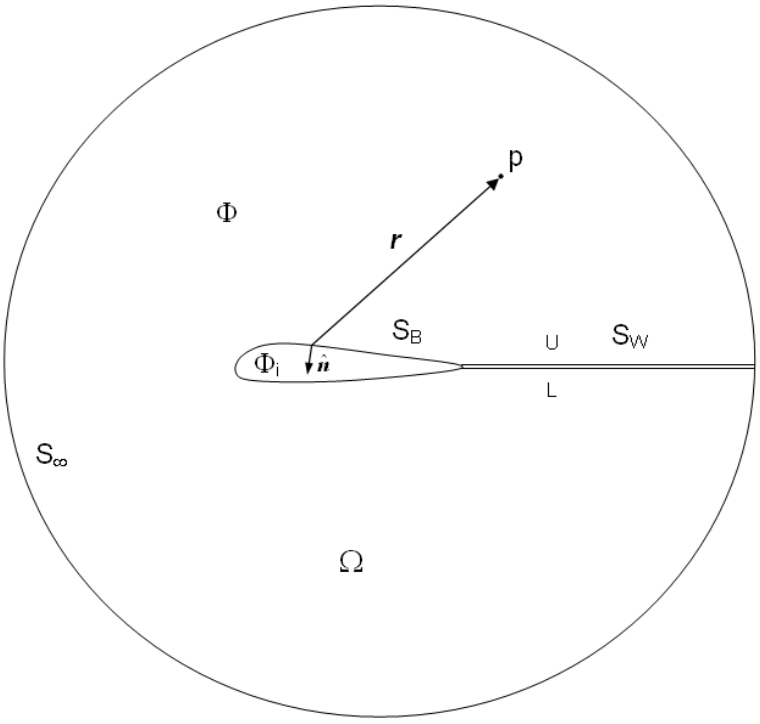

Figure 1. A section of the analysis domain passing through the aerodynamic body and its wake.

For the typical arrangement described above, a general solution for the velocity potential at any point *p*, in either flow region, can be constructed in terms of surface integrals of the velocity potential and its derivatives by applying Green's theorem [1]. This procedure yields

$$\begin{aligned}\Phi_p = &-\frac{1}{4\pi}\iint_{S_B}(\Phi-\Phi_i)\nabla\left(\frac{1}{r}\right)\cdot\hat{\boldsymbol{n}}\,dS + \frac{1}{4\pi}\iint_{S_B}\left(\frac{1}{r}\right)\nabla\left(\Phi-\Phi_i\right)\cdot\hat{\boldsymbol{n}}\,dS \\ &-\frac{1}{4\pi}\iint_{S_W}\left(\Phi_U-\Phi_L\right)\nabla\left(\frac{1}{r}\right)\cdot\hat{\boldsymbol{n}}\,dS + \phi_\infty(\mathrm{p})\end{aligned} \tag{7}$$

where r is the distance between the point p and a differential surface element dS having normal vector $\hat{\boldsymbol{n}}$, ϕ_∞ is a constant freestream potential at point p due to S_∞ (the fluid surrounding the body is assumed to be stationary in the inertial frame) and the wake is considered to be thin enough so that the jump in the normal component of the velocity across the same is zero (flow entrainment in the wake is neglected). Note that the total velocity potential in Eq. (7) can be seen as being composed of a freestream potential ϕ_∞ plus a perturbation potential due to the body and its wake, given by $\phi = \Phi - \phi_\infty$. Next, defining the jump in velocity potential across the boundary as a doublet distribution with strength $-\mu = \Phi - \Phi_i$ and the jump in the normal component of the velocity as a source distribution with strength $-\sigma = \nabla(\Phi - \Phi_i)\cdot\hat{\boldsymbol{n}}$, Eq. (7) can be rewritten as

$$\Phi_p = \frac{1}{4\pi}\iint_{S_B} \mu \nabla\left(\frac{1}{r}\right)\cdot\hat{\boldsymbol{n}}\, dS - \frac{1}{4\pi}\iint_{S_B}\left(\frac{\sigma}{r}\right) dS + \frac{1}{4\pi}\iint_{S_W} \mu_W \nabla\left(\frac{1}{r}\right)\cdot\hat{\boldsymbol{n}}\, dS + \phi_\infty(\mathrm{p}) \tag{8}$$

being $\mu_W = \Phi_U - \Phi_L$ the jump in potential across the wake. The solution of Eq. (8) reduces to find a suitable distribution of doublets and sources along the body and its wake satisfying the boundary conditions (b) and (c). Note that the far-field condition (a) is automatically satisfied by Eq. (8) as the perturbation potential tends to zero when $r \to \infty$.

In order to satisfy Neumann conditions (b), the velocity across the boundaries can be directly specified by enforcing Eq. (6) or a similar effect can be achieved indirectly by modeling the flow inside the body (classical approaches are discussed in [5]). In this work, the internal Dirichlet condition $\Phi_i = const. = \phi_\infty$ is applied [1, 5]. Accordingly, the doublet strength -μ turns into the perturbation velocity potential

$$-\mu = \phi = \Phi - \phi_\infty \tag{9}$$

and the source strength results

$$-\sigma = \nabla(\Phi - \phi_\infty)\cdot\hat{\boldsymbol{n}} \tag{10}$$

Then, introducing Eqs. (9) and (10) into Eq.(8), the total potential inside the body becomes

$$0 = \frac{1}{4\pi}\iint_{S_B} \mu \nabla\left(\frac{1}{r}\right)\cdot\hat{\boldsymbol{n}}\, dS - \frac{1}{4\pi}\iint_{S_B}\left(\frac{\sigma}{r}\right) dS + \frac{1}{4\pi}\iint_{S_W} \mu_W \nabla\left(\frac{1}{r}\right)\cdot\hat{\boldsymbol{n}}\, dS \tag{11}$$

and the source strengths are determined by replacing $\hat{\boldsymbol{n}}\cdot\nabla\Phi$ from Eq. (6) in Eq. (10). Hence,

$$\sigma = -\mathrm{V_N} - \left(\mathbf{V}_0 + \boldsymbol{\omega}\times\boldsymbol{r} + \mathbf{v}_{rel}\right)\cdot\hat{\boldsymbol{n}} \tag{12}$$

and the internal Dirichlet boundary condition, given by Eq. (11), can be solved for the unknown body doublet distribution (the wake doublicity will be determined by the Kutta condition). The flow field around thick body configurations having an internal volume enclosed by boundaries S_B is solved on the base of this equation.

Usually, it is of interest in aerodynamic analyses to deal with component parts or bodies which are extremely thin (e.g. relative thickness < 1% [5]). In such cases, the upper and lower sides of the boundary are collapsed into a sheet across the same the normal component of the velocity is assumed to be continuous. An equation for modeling thin boundaries is achieved at a given point *p* by replacing the perturbation velocity, obtained by differentiating Eq.(8), into the Neumann condition given by Eq. (6). This yields,

$$\frac{1}{4\pi}\iint_{S_B}\mu\,\hat{\boldsymbol{n}}_p\cdot\nabla\left(\hat{\boldsymbol{n}}\cdot\nabla\left(\frac{1}{r}\right)\right)dS + \frac{1}{4\pi}\iint_{S_W}\mu_W\,\hat{\boldsymbol{n}}_p\cdot\nabla\left(\hat{\boldsymbol{n}}\cdot\nabla\left(\frac{1}{r}\right)\right)dS - \hat{\boldsymbol{n}}_p\cdot\mathbf{v} = \mathrm{V_{N_P}} \tag{13}$$

which can be solved for the doublet distribution on thin aerodynamic surfaces. Note that the source contributions are zero in Eq. (13) as the normal component of the velocity is assumed to be constant across thin boundaries. However, if aerodynamic configurations having mixed thin/thick surfaces are considered, the contribution to the normal component of the velocity due to the source distribution on thick boundaries must be accounted for in Eq. (13).

3.1 Wake modeling

As mentioned in Section 2, the solution of lifting problems is not uniquely determined unless the circulation Γ around the body is fixed. If we take a close path line around a spanwise section along the body, the circulation can be related with the jump in velocity potential across the wake by means of [1]

$$\Gamma = \left(\Phi_U - \Phi_L\right)_W = \mu_W \tag{14}$$

Therefore, given the fact that circulation is related to lift by the Kutta-Joukowski theorem, a proper wake doublicity μ_W must be specified in order to obtain realistic solutions for lifting aerodynamic problems (notice that no wake is needed for non-lifting problems as $\Gamma = 0$). With this purpose, the Kutta condition (c) is applied.

In 2D lifting airfoil problems, the Kutta condition can be met by setting the vorticity at the trailing edge to zero, i.e. $\gamma_{TE} = 0$. Moreover, since the component of vorticity in the flow

direction s is related to the doublet strength by $\gamma(s) = -\partial\mu/\partial s$, the condition $\mu_{TE} = \mu_W = const.$ must also be satisfied at the trailing edge. These results can be extrapolated to the 3D case in order to determine the doublicity shed into the wake. This is accomplished by forcing zero total vorticity at each spanwise station along the trailing edge (shedding line) through

$$\mu_{TE_U} - \mu_{TE_L} - \mu_W = 0 \tag{15}$$

where μ_{TE_U} and μ_{TE_L} are the doublet strength at the upper and lower surfaces of the trailing edge respectively and μ_W is the unknown wake doublet strength next to the trailing edge (the shedding line location is assumed to be known and determined by the body and flow geometry). Moreover, the doublicity μ_W obtained from Eq. (15) must remain constant along mean streamlines in the wake surface in order to satisfy vorticity conservation theorems. It should be noticed that condition (15) turns into $\mu_{TE} - \mu_W = 0$ for thin boundaries.

As long as wake shape is concerned, it is determined by considering a differential surface element in the wake dS_W and evaluating the elemental aerodynamic force acting on it. In virtue of the Kutta-Joukowski theorem, this elementary force is

$$d\boldsymbol{F} = \rho \boldsymbol{V} \times \boldsymbol{\gamma}\, dS_W \tag{16}$$

with ρ and **V** being the density and local mean velocity of the flow respectively. As no force can act on a wake surface element, from Eq. (16) it follows that

$$\boldsymbol{V} \times \boldsymbol{\gamma} = 0 \tag{17}$$

hence, the vorticity vector must be parallel to the velocity at any point on the wake surface. In other words, the wake surface must be parallel to the local streamlines of the flow.

Due to the fact that the wake shape depends on the velocity field which, in turn, depends on the wake shape (this must be known when computing Eq. (11) or Eq. (13)), an iterative approach seems to be necessary for obtaining the solution of the problem. A typical iterative scheme is the wake-relaxation method employed in [5]. In the present work, the non-linearity is avoided by adopting a time-steeping procedure [2, 6] where a free-wake is developed according to the motion of the body as the solution advances in time. We will come back to this point later on in Section 4.2.

4. NUMERICAL SOLUTION

The aerodynamic analysis of arbitrary configurations is carried out by solving a discrete version of the governing integral equations (11) and (13) in a numerical manner. With this aim, the body boundaries S_B are discretized into N_B triangular or quadrilateral flat surface panels forming a surface grid. The wake surface S_W is assumed to be composed of N_W quadrilateral panels developing from specified shedding lines on the body. Each panel is identified by its corner points, a particular point named *control point* and a local coordinates system. The control point is located at the centroid of the panel, on the surface or slightly inside the body. The panel coordinate system, whose origin is located at the control point, is defined by a unit outward normal vector $\hat{\boldsymbol{n}}$ and a set of unit tangent vectors $\hat{\boldsymbol{l}}$ and $\hat{\boldsymbol{m}}$. A typical panel discretization for a wing-body configuration is shown in Figure 2.

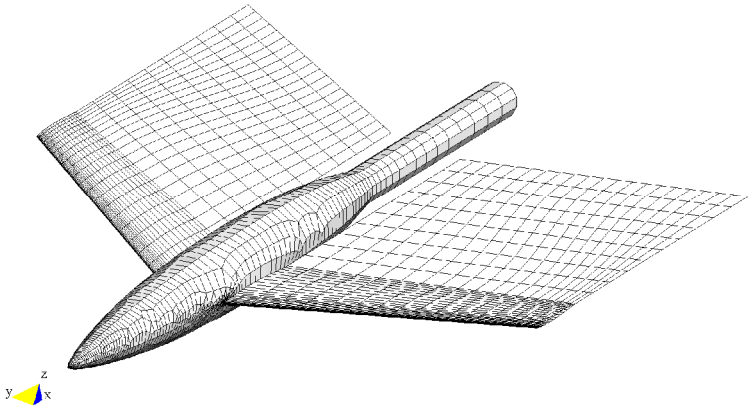

Figure 2. Typical wing-body and wake discretization.

The discretized form of the integral governing equations is achieved by breaking down the surface integrals over S_B and S_W into integrals over the panels. Assuming that the doublet and source strength is constant on each panel (low-order method), these terms can be factored out of the panel integrals allowing the latter to be solved in a closed manner. Then, the discrete equations are satisfied at each control point $J = 1, N_B$ on the body by considering all panels contributions $K = 1, N_B + N_W$. According to this procedure, the discrete version of the internal Dirichlet condition (Eq. (11)) is set at each control point $J = 1, N_B^{thick}$ on thick boundaries by

$$\sum_{K=1}^{N_B} \mu_K C_{JK} + \sum_{L=1}^{N_W} \mu_L C_{JL} = \sum_{K=1}^{N_B} \sigma_K B_{JK} \tag{18}$$

where C_{JK} and B_{JK} denote, respectively, the perturbation potential (per unit strength) due to a constant doublet and source distribution on panel K acting on a control point J. These influence coefficients are given by

$$C_{JK} = \iint_{S_K} \nabla_K \left(\frac{1}{r_{JK}} \right) \hat{\boldsymbol{n}}_K \, dS_K \tag{19}$$

$$B_{JK} = \iint_{S_K} \frac{1}{r_{JK}} dS_K \tag{20}$$

being $\hat{\boldsymbol{n}}_K$ and dS_K the normal vector and a differential surface area of panel *K* respectively. The distance r_{JK} is measured from the control point *K* to the control point *J*, i.e. $r_{JK} = \left\| \boldsymbol{x}_J - \boldsymbol{x}_K \right\|$ and the gradient is computed with respect to the coordinates of panel *K*. It should be pointed out that the surface integrals become singular when $r_{JK} \to 0$. For that special case, a slightly different approach is followed when deriving Eq. (7) leading to $\Phi_p = -(\Phi - \Phi_i)/2 = \mu/2$ when *p* is inside the body (see for instance [1]). Accordingly, $C_{JJ} = 2\pi$ is set in Eq. (18) when evaluating the panel influence on itself.

Similarly, Eq. (13) is discretized for each control point $j = 1, N_B^{thin}$ on thin surfaces as

$$\sum_{K=1}^{N_B} \mu_K E_{JK} + \sum_{L=1}^{N_W} \mu_L E_{JL} = \sum_{K=1}^{N_B} \sigma_K D_{JK} + \hat{\boldsymbol{n}}_J \cdot \mathbf{v} + V_{N_J} \tag{21}$$

where **v** is the instantaneous kinematic velocity given by Eq.(5), V_{NJ} denotes a prescribed normal velocity relative to the boundary and $\hat{\boldsymbol{n}}_J$ is the unit normal vector at the control point *J*. The normal components of the perturbation velocity at control point *J* due to a constant doublet and source distribution (per unit strength) on panel *K* are obtained as

$$E_{JK} = \hat{\boldsymbol{n}}_J \cdot \mathbf{V}_{\mu_{JK}} \tag{22}$$

$$D_{JK} = \hat{\boldsymbol{n}}_J \cdot \mathbf{V}_{\sigma_{JK}} \tag{23}$$

with

$$\mathbf{V}_{\mu_{JK}} = \frac{1}{4\pi} \iint_{S_K} \nabla_J \left(\hat{\boldsymbol{n}}_K \cdot \nabla_K \left(\frac{1}{r_{JK}} \right) \right) dS_K \tag{24}$$

$$\mathbf{V}_{\sigma_{JK}} = \frac{1}{4\pi} \iint_{S_K} \nabla_J \left(\frac{1}{r_{JK}} \right) dS_K \tag{25}$$

In spite of the fact that the source distribution vanishes for thin surface panels as there is no jump in the normal velocity across these boundaries (see Eq. (13)), the influence coefficient D_{JK} is included in the discrete Eq. (21) to account for the perturbation velocity induced on

thin panels by source distributions placed on thick panels (for configurations presenting mixed thin/thick boundaries).

4.1 Calculation of the influence coefficients

The influence coefficients, given by Eqs. (19) and (20) for the velocity potential and Eqs. (24) and (25) for the velocity vector, are computed in a closed manner following the procedure presented in [5]. In that work, the integrals on a given panel are evaluated by adding individual contributions of its sides (rounded in a counter-clockwise sense) and this fact allows quadrilateral and triangular panels (as a matter of fact any closed polygonal panel) to be treated in a similar manner.

The geometrical model employed for the calculations is presented in Figure 3. Each panel is geometrically defined by its corner points $\mathbf{R}_1$, $\mathbf{R}_2$,..,$\mathbf{R}_n$ (numbered in a counter-clockwise sense according to the panel's outward normal vector), the control point $\mathbf{R}_C$ (given by $\left(\sum_{i=1}^{n}\mathbf{R}_i\right)/n$) and a set of unit normal and tangent vectors. The normal vector $\boldsymbol{n}$ is computed by the cross product of the panel's diagonals. The first tangent vector $\boldsymbol{m}$ is generated between the control point and the mid-point of one of the panel sides (e.g. in a quadrilateral panel $\boldsymbol{m} = (\boldsymbol{R}_3 + \boldsymbol{R}_4)/2 - \boldsymbol{R}_C$) and the second tangent vector $\boldsymbol{l}$ is defined to be orthogonal to $\boldsymbol{m}$ and $\boldsymbol{n}$, i.e $\boldsymbol{l} = \boldsymbol{m} \times \boldsymbol{n}$. Then, these vectors are normalized ($\hat{}$).

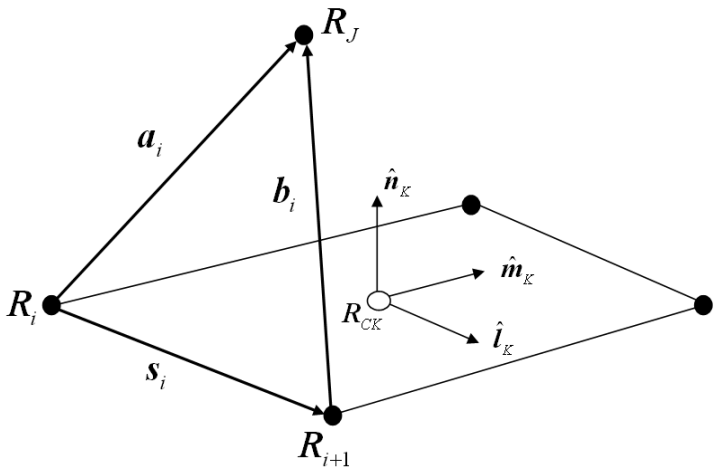

Figure 3. Geometrical arrangement for the evaluation of the panel influence coefficients.

The influence of a panel *K* on a point *J* is computed exclusively by the geometry of the panel and the coordinates of the point where the panel's influence is sought. Previous to the calculations, the panel corner points $\mathbf{R}_i$ and the point $\mathbf{R}_J$ are converted to the panel local system, defined by the unit vectors $(\hat{\boldsymbol{l}}_K, \hat{\boldsymbol{m}}_K, \hat{\boldsymbol{n}}_K)$, with origin at the control point $\mathbf{R}_{CK}$. Then,

each panel side is defined as $\boldsymbol{s}_i = \boldsymbol{R}_{i+1} - \boldsymbol{R}_i$ and three auxiliary vectors are introduced: $\boldsymbol{a}_i = \boldsymbol{R}_J - \boldsymbol{R}_i$, $\boldsymbol{b}_i = \boldsymbol{R}_J - \boldsymbol{R}_{i+1}$ and $\boldsymbol{P}_{JK} = \boldsymbol{R}_J - \boldsymbol{R}_{CK} = \boldsymbol{R}_J$ (in panel coordinates). Note that $\boldsymbol{a}_i = \boldsymbol{b}_{i-1}$ when the panel is rounded in a counter-clockwise sense.

Following the former definitions, the influence coefficients for constant strength doublet and source panels are computed. In this work we will focus on the final expressions for the sake of brevity. Derivation details can be found in [5] and the references cited therein.

4.1.1 Velocity potential influence coefficients

The velocity potential at a given point *J* due to a unit doublet constant distribution on panel *K* is given by Eq. (19). This integral term can be computed as

$$C_{JK} = \sum_{i=1,n} C_{JK_i} \tag{26}$$

where C_{JK_i} is the contribution of each panel side $\mathbf{s}_i$. Following VSAERO [5] nomenclature,

$$\mathrm{C}_{\mathrm{JK}_i} = \tan^{-1}\left(\frac{RNUM}{DNOM}\right) \tag{27}$$

with

$$\begin{aligned} RNUM &= SM * PN * (B * PA - A * PB) \\ DNOM &= PA * PB + PN^2 * A * B * SM^2 \end{aligned} \tag{28}$$

where

$$\begin{aligned} PN &= \boldsymbol{P}_{JK} \cdot \hat{\boldsymbol{n}}_K \quad (= P_{JK}(3)) \\ A &= \|\boldsymbol{a}_i\| \\ B &= \|\boldsymbol{b}_i\| \\ PA &= PN^2 * SL + A1 * AM \quad (= \boldsymbol{a}_i \cdot [\hat{\boldsymbol{l}}_K \times (\boldsymbol{a}_i \times \boldsymbol{s}_i)] \\ PB &= PN^2 * SL + A1 * BM = PA - A1 * SM \\ A1 &= AM * SL - AL * SM \quad (= \hat{\boldsymbol{n}}_K \cdot (\boldsymbol{s}_i \times \boldsymbol{a}_i)) \\ SL &= \boldsymbol{s}_i \cdot \hat{\boldsymbol{l}}_K \quad (= s_1) \\ AL &= \boldsymbol{a}_i \cdot \hat{\boldsymbol{l}}_K \quad (= a_1) \\ SM &= \boldsymbol{s}_i \cdot \hat{\boldsymbol{m}}_K \quad (= s_2) \\ AM &= \boldsymbol{a}_i \cdot \hat{\boldsymbol{m}}_K \quad (= a_2) \\ BM &= \boldsymbol{b}_i \cdot \hat{\boldsymbol{m}}_K \quad (= b_2) \end{aligned} \tag{29}$$

Following a similar approach, the velocity potential at a given point *J* due to a unit constant strength on panel *K*, given by Eq. (20), is computed by

$$B_{JK} = \sum_{i=1,n} B_{JK_i} \tag{30}$$

being the contribution of each panel side $\mathbf{s}_i$

$$B_{JK_i} = A1 * GL - PN * C_{JK_i} \tag{31}$$

where *A1* and *PN* are given in (29), the doublet side contribution C_{JK_i} in Eq. (27) and

$$GL = \frac{1}{s} \log \left| \frac{A + B + s}{A + B - s} \right| \tag{32}$$

with $s = \|\boldsymbol{s}_i\|$.

If the point *J* is far from panel *K*, far-field approximations are employed for computing the influence coefficients in order to reduce computational cost. In such a case, the distributed singularity on panel *K* is treated as if it was a point singularity and the influence coefficients result [5]

$$C_{JK} = \frac{PN * A_K}{P_{JK}^3} \quad , \quad B_{JK} = \frac{A_K}{P_{JK}} \tag{33}$$

where $P_{JK} = \|\boldsymbol{P}_{JK}\|$ is the distance between the control point *K* and point *J*, A_K denotes the surface area of panel *K* and *PN* is given in (29). These approximations reduce the computational cost considerably when computing the influence coefficients without affecting solution accuracy. In this work, far-field approximations are used when $P_{JK} > c_1 h_K$, being c_1 a constant parameter (typically 5) and h_K a characteristic length, computed at each panel as the maximum of the distances between the control point and the sides' mid-point.

4.1.2 Velocity vector influence coefficients

The velocity induced at a given point *J* due to a unit doublet distribution on panel *K* is given by Eq. (24). Similarly to the velocity potential, this integral can be computed by [5]

$$\mathbf{V}_{\mu_{JK}} = \frac{1}{4\pi} \sum_{i=1,n} \mathbf{V}_{\mu_{JK_i}} \tag{34}$$

being each panel side contribution

$$\mathbf{V}_{\mu_{JK_i}} = \frac{\boldsymbol{a}_i \times \boldsymbol{b}_i * (A + B)}{A * B * (A * B + \boldsymbol{a}_i \cdot \boldsymbol{b}_i)} \tag{35}$$

where all the variables involved have been defined in (29). Note that a finite-core model can be applied to avoid singularities in Eq. (35) when it is evaluated on panel's sides [1, 5].

The velocity induced at point *J* by a unit constant source distribution on panel *K* results

$$\mathbf{V}_{\sigma_{JK}} = \frac{1}{4\pi} \sum_{i=1,n} \mathbf{V}_{\sigma_{JK_i}} \tag{36}$$

being the side contribution

$$\mathbf{V}_{\sigma_{JK_i}} = GL * (SM * \hat{\boldsymbol{l}}_K - SL * \hat{\boldsymbol{m}}_K) + C_{JK_i} * \hat{\boldsymbol{n}}_K \tag{37}$$

where *GL* is given by Eq. (32), C_{JK_i} by Eq. (27) and the rest of variables are defined in (29).

Similarly to the perturbation potentials, if the point of interest *J* is located far from panel *K* the induced velocities can be approximated by far-field formulae resulting in

$$\begin{aligned} \mathbf{V}_{\mu_{JK}} &= \frac{A_K}{P_{JK}^5} * \left(3 * PN * \boldsymbol{P}_{JK} - P_{JK}^2 * \hat{\boldsymbol{n}}_K\right) \\ \mathbf{V}_{\sigma_{JK}} &= \frac{A_K}{P_{JK}^3} * \boldsymbol{P}_{JK} \end{aligned} \tag{38}$$

being A_K the surface area of panel *K*.

4.2 Time-marching wake development procedure

The unsteady solution of the discrete governing equations (18) and (21) along with Eq. (6) is carried out in a series of time steps. It is considered that the body is initially at rest for $t = t_0 = 0$ and the velocity of the body origin $\mathbf{V}_0(t)$ and the orientation angles $\boldsymbol{\Theta}(t)$ (or the rates of rotation $\boldsymbol{\Omega}(t)$) are known for $t > t_0$. Then, the solution proceeds as follows.

At the first time step, the simulation time is increased by a prescribed time increment Δt. In consequence, the body is displaced from its original position according to the flight path and a first row of wake panels is shed into the wake from specified shedding lines on the body (trailing edges, tips, etc.). Notice that we will refer to any shedding line as a trailing edge. Then, the strengths of the shed panels are written in terms of the body doublets by enforcing the Kutta condition (15), and the linear system resulting from applying Eqs. (18) and (21) at the body's control points can be solved for the unknown body doublets (see [1] for implementation details). Once the body doublicity is known, the velocity field and the aerodynamic loads acting on the body at time $t_1 = \Delta t$ can be computed. Note that in case an impulsively start of the body is required, the solution at time t_0 (for which no wake exists) is computed prior to setting the body into motion. As stated in Section 3.1, once a wake panel is shed, it must remain parallel to the local streamlines of the flow. As the inertial frame is

defined to be at rest, the only velocities acting on a shed panel are those induced by the body and wake panels. Therefore, in order to align a wake panel with the local flow (wake rollup), the total induced velocity acting on the panel's corner points is computed in the inertial frame and the coordinates of these points are translated according to $(\Delta x, \Delta y, \Delta z) = (u, v, w)_{ind} \Delta t$. The total induced velocity at each point is obtained by adding all the doublet and source panel contributions given by Eqs. (34) and (36).

Afterwards, the time step is increased and $t_2 = t_1 + \Delta t$. The body is moved again and a new row of wake panels is shed into the wake, linking the panels at the body's trailing edge with those previously convected at time $t = t_1$. Then, the doublet distribution for the new row of wake panels is related to the body doublicity by applying the Kutta condition at the trailing edges. In addition, as the doublicity of the panels shed before into the wake (at time $t = t_1$) must remain constant, their contributions to Eqs. (18) and (21) are already known and can be translated to the right hand side. Next, the equations system is solved for the body doublet distribution at time $t = t_2$, the velocity field and the loads acting on the body are computed and the wake rollup procedure is performed for all the wake panels. These basic steps are carried out at each time step until the final simulation time is reached.

4.3 Further implementation remarks

The body panels influence coefficients are constant unless the body geometry changes in the fixed frame. As a result, these terms can be computed once, at the first time step, and stored in such a way that only the wake contributions are updated in the following time steps.

The linear system resulting from satisfying Eqs. (18) and (21) at the body's control points is solved by using a Bi-Conjugate Gradient method (BiCG). As the system solution at each time step is started with the doublet distribution computed at the previous time step, only a few solver iterations are needed for updating the unknowns, which keeps the computational cost low. Due to the fact that the system matrix is full, there are no advantages concerning storage. This is an important drawback that limits the number of panels to be employed according to the physical memory available and computer memory management issues. In order to overcome this restriction, simple-precision data storage can be adopted. In addition, the application of matrix lumping techniques (see for instance [7]) seems to be an attractive solution, although its feasibility in the present context should be investigated further.

Most of the computational effort in panel techniques is involved in the calculation of the influence coefficients and this is a task which can be safely executed in parallel, given the fact that these coefficients are completely independent from each other. Consequently, large speedups can be expected to be achieved.

5. AERODYNAMIC LOADS

The solution of Eqs. (18) and (21) provides the unknown doublet distribution on the body. As the doublet strength is related to jumps in the velocity potential across the boundaries, the velocity field on the body can be computed by numerical differentiation of the doublet distribution. Then, the pressure distribution can be determined from the velocity field by applying Bernoulli's equation, after which the calculation of the aerodynamic loads acting on the body is straightforward.

5.1 The unsteady Bernoulli's equation

The unsteady Bernoulli's equation results from integrating the momentum conservation equations in space. For an incompressible, inviscid and irrotational flow this yields [1]

$$\frac{\partial \Phi}{\partial t} + \frac{\mathrm{V}^2}{2} + \frac{p}{\rho} = C(t) \tag{39}$$

where V, p and ρ denote, respectively, the magnitude of the local velocity, the pressure and the density; $C(t)$ is a time-dependent constant and body forces have been omitted. Next, Eq. (39) can be evaluated for the same time instant t at both, an arbitrary and a reference far-field point. Equating the resulting expressions it is possible to obtain

$$\frac{p - p_\infty}{\rho_\infty} = \frac{\mathrm{V}_\infty^2}{2} - \frac{\mathrm{V}^2}{2} - \frac{\partial \phi}{\partial t} \tag{40}$$

where $\phi = \Phi - \phi_\infty$ and $\rho = \rho_\infty$ (incompressible fluid). As can be observed, Eq. (40) enables the computation of the pressure at any arbitrary point in the fluid in terms of the velocity. Therefore, the coefficient of pressure (Cp) can be calculated at any point as

$$Cp = \frac{p - p_\infty}{1/2\, \rho_\infty \mathrm{V}_\infty^2} = 1 - \left(\frac{\mathrm{V}}{\mathrm{V}_\infty} \right)^2 - \frac{2}{\mathrm{V}_\infty^2} \frac{\partial \phi}{\partial t} \tag{41}$$

and this equation is applied for computing the aerodynamic loads acting on thick and thin body surface panels.

In the following, we consider the velocity vector to act on the panel's control point, the pressure to be constant on each panel and the resultant aerodynamic force also to be applied at the panel's control point. V is defined as the magnitude of the total velocity at the control point (kinematic + perturbation) and V_∞ is the magnitude of a reference freestream velocity. According to the problem to be solved, the latter can be assumed to be equal to the body translation velocity $\|\mathbf{V}_0\|$ or equal to the local kinematic velocity (Eq. (5)). The reference pressure p_∞ and density ρ_∞ correspond to known far-field boundary conditions.

5.2 Thick body panels treatment

For a surface panel *K* belonging to thick boundaries, the perturbation velocity potential coincides with the panel's doublet strength and the components of the perturbation velocity vector can be evaluated by taking the gradient of μ in panel coordinates. Hence, the tangential components of the perturbation velocity vector result

$$q_l = \frac{\partial \mu}{\partial \hat{\boldsymbol{l}}} \quad , \quad q_m = \frac{\partial \mu}{\partial \hat{\boldsymbol{m}}} \tag{42}$$

and the normal component of the velocity is given by

$$q_n = \sigma \tag{43}$$

being σ the panel's source strength (12). The total velocity on panel *K* is obtained by adding the perturbation velocity to the instantaneous local kinematic velocity, i.e.

$$\mathbf{V} = q_l * \hat{\boldsymbol{l}} + q_m * \hat{\boldsymbol{m}} + q_n * \hat{\boldsymbol{n}} + \left(\mathbf{V}_0 + \boldsymbol{\omega} \times \boldsymbol{r} + \mathbf{v}_{rel}\right) \tag{44}$$

In spite of the fact that the evaluation of Eqs. (42) can be easily performed on structured discretizations by using finite difference approximations [2, 5], arbitrary body discretizations demand a more general approach. In this work the derivatives are evaluated at each panel using the value of the doublet strength at the panel's corner points *i*. These *a-priori* unknown values are approximated at each corner point *i* by means of a smoothing procedure

$$\mu^i = \frac{\sum_{j=1,ns_i} A_J \mu_J}{\sum_{j=1,ns_i} A_J} \tag{45}$$

where A_J and μ_J are the surface area and doublet strength of a panel *J* respectively and the summation is performed for the ns_i panels surrounding a corner point *i*. It should be noticed that discontinuities in the doublet strength distribution must be avoided when computing Eq.

(45). This is likely to occur when the point lies on a shedding line. In that case, a criterion based on the surface normal vectors is applied to determine which panels are included in the summation and which are not. Once the doublet strengths at the panel's corner points are determined, the derivatives (42) are evaluated (in panel coordinates) by using a standard finite element approximation.

Once the total velocity vector (Eq. (44)) is known, the elemental aerodynamic force acting on each panel can be determined by

$$\Delta \mathbf{F}_K = -Cp_K * A_K * q_\infty * \hat{\boldsymbol{n}}_K \tag{46}$$

where A_K and $\hat{\boldsymbol{n}}_K$ are the surface area and unit normal vector of panel K respectively, Cp_K is the pressure coefficient (computed according to Eq. (41) with $\partial\phi/\partial t = -\partial\mu/\partial t = -(\mu_t - \mu_{t-\Delta t})/\Delta t$) and q_∞ is a reference freestream dynamic pressure. Then, the elemental aerodynamic moment coefficient is calculated as

$$\Delta \mathbf{M}_K = \boldsymbol{r}_K \times \Delta \mathbf{F}_K \tag{47}$$

being $\boldsymbol{r}_K(x, y, z)$ the vector distance between the panel's control point and the reference point about the same the aerodynamic moment is desired. The total aerodynamic force and moment coefficient for the analysis configuration are computed by adding elemental panel contributions

$$\begin{aligned} \mathrm{C}_{\mathbf{F}} &= \left[C_x, C_y, C_z \right]^{\mathrm{T}} = \frac{1}{q_\infty * S_{ref}} \sum_{K=1}^{N_B} \Delta \mathbf{F}_K \\ \mathrm{C}_{\mathbf{M}} &= \left[C_{M_x}, C_{M_y}, C_{M_z} \right]^{\mathrm{T}} = \frac{1}{q_\infty * S_{ref} * L_{ref}} \sum_{K=1}^{N_B} \Delta \mathbf{M}_K \end{aligned} \tag{48}$$

where S_{ref} and L_{ref} (reference surface area and length) are specified according to the problem under study.

5.3 Thin body panels treatment

The doublet strength on thin boundaries is related to the jump in velocity potential across the sheet by $\mu = \Phi_U - \Phi_L$ and the source strength becomes zero in order to satisfy continuity in the normal velocity component. Hence, the gradient of the doublet strength provides the jump in the tangential velocity across the panel, i.e.

$$\Delta \mathbf{V}_t = \mathbf{V}_t^U - \mathbf{V}_t^L = \nabla \mu \tag{49}$$

The tangential components of the total velocity can be obtained by

$$\begin{aligned} \mathbf{V}_t^U &= \mathbf{V}_a + \tfrac{1}{2}\Delta\mathbf{V}_t \\ \mathbf{V}_t^L &= \mathbf{V}_a - \tfrac{1}{2}\Delta\mathbf{V}_t \end{aligned} \tag{50}$$

being $\mathbf{V}_a$ an averaged tangential velocity at the panel's control point (kinematic + perturbation) that omits the panel contribution on itself. Therefore, the net pressure acting on the panel can be computed by replacing Eqs. (50) with (49) in Eq. (41). This leads to

$$\Delta Cp = Cp^U - Cp^L = -\frac{2}{\mathrm{V}_\infty^2}\left(\mathbf{V}_a \cdot \Delta\mathbf{V}_t + \frac{\partial\mu}{\partial t}\right) \tag{51}$$

and the elemental aerodynamic force and moment contributions are obtained by Eqs. (46) and (47). Like in the thick panels procedure, the elemental contributions are added in Eqs. (48) to obtain force and moment coefficients acting on the body.

It must be noticed that the smoothing procedure given by Eq. (45) may render not enough-accurate representations of the nodal doublicity near leading edges and tips belonging to thin surfaces, causing an underestimation of the gradient at these panels. In those cases, an improved recovery of the nodal doublicity must be applied. In this work, with the aim of keeping the computations as general as possible, avoiding additional verifications of panels ordering and other geometrical features, an alternative procedure is adopted. Hence, the jump in the tangential velocity across a thin panel *k* (Eq. (49)) is approximated by

$$\Delta\mathbf{V}_{t_k} = \tfrac{1}{2}\,\hat{\boldsymbol{n}}_k \times \boldsymbol{\Omega}_k \tag{52}$$

where $\boldsymbol{\Omega}_k$ represents an averaged panel circulation computed as

$$\boldsymbol{\Omega}_k = \frac{1}{A_k}\sum_i \gamma_i \boldsymbol{s}_i \tag{53}$$

being $\boldsymbol{s}_i$, $i=1,n$ a panel side vector (see Figure 3) and γ_i the circulation along that side. The latter is obtained as the difference of the circulations (doublet strengths) of neighbouring panels sharing the side $\boldsymbol{s}_i$. This procedure also facilitates the computation of the tangential force components acting on a thin panel by applying the Kutta-Joukowsky theorem along its sides. To this end, the total velocity is evaluated at each control point and assumed to be constant along the panel. This simplification reduces the computational effort without degrading the accuracy of the results.

6. APPLICATION EXAMPLES

In this section three test cases are presented with the aim of assessing the performance of the present methodology. The first example is an unsteady analysis concerning the impulsive set into motion of a rectangular low aspect ratio wing. The second one involves a stationary flow around a NACA wing-body configuration and the third test case focuses again on another unsteady computation regarding a hovering two-blades rotor. The computed solutions are compared with experimental and numerical reference results reported in the literature.

6.1 Impulsive movement of a rectangular wing

This example analyzes the behaviour of a rectangular wing, originally at rest, which is spontaneously set into movement. The wing has a NACA 0012 airfoil constant along the span and an aspect ratio A = 4. The discretization consists of 25 quadrilateral panels in the chordwise direction and other 35 along the span (1750 panels). In order to perform the simulation, an initial non-dimensional time increment $\Delta t^* = U_\infty \Delta t / c = 0.025$ and an angle of attack α = 5º are adopted. With the aim of getting a faster convergence to the stationary solution of the problem, the time increment is gradually increased some time units after the wing is set into motion. Figure 4 depicts the unsteady wake developed behind the wing, as it moves in the stationary air, for different instant times during the simulation. The wing starting vortex can be observed.

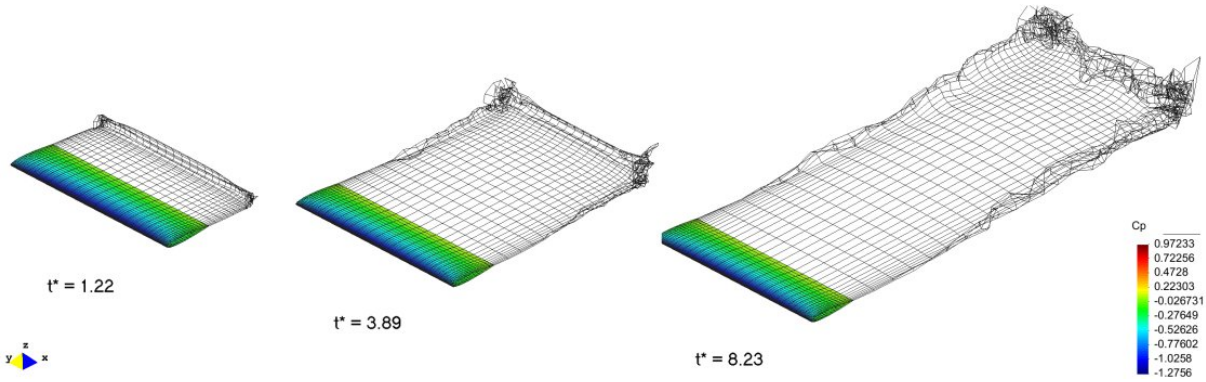

Figure 4. Wing and wake snapshots at different instant times after the wing is impulsively set into motion. Cp results are displayed (A=4 and α=5º).

The unsteady lift coefficient of the wing (C_L) is computed and the results are plotted in Figure 5 together with some discrete points taken from [1]. A good agreement can be observed between the results, although the stationary lift coefficient obtained in our computation seems to be slightly lower than that obtained in [1]. However, it should be noticed that in that reference an unsteady vortex lattice method is employed and the wing is discretized with 4

panels along the chord and 30 equally spaced panels in the spanwise direction. This could be a possible reason accounting for slight differences between the results.

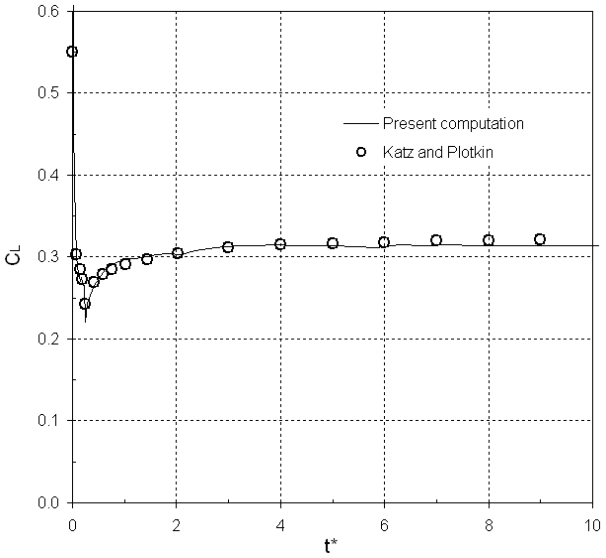

Figure 5. Unsteady lift coefficient for a rectangular wing impulsively set into motion (A=4 and α=5º).

6.2 Steady analysis of a NACA wing-body configuration

The flow around a symmetric NACA wing-body is solved in this example and the numerical results are compared with experimental measurements reported in [8]. The wing has a sweepback $\Lambda_{1/4}$ = 45º, an aspect ratio A = 4, a taper ratio λ = 0.6 and it has no geometrical twist. The wing-section is a NACA 65A006 airfoil constant along the wing span. The fuselage has a circular cross-section and its rear part is attached to a sting which supports the model in the wind tunnel test section. The problem discretization, shown in Figure 6, consists of a structure distribution of 3200 quadrilateral panels (only quadrilateral panels are employed as they offer a better performance than triangular panels). The wing is discretized by 45 panels in the chordwise direction, 40 panels along the span and no matching panels are used in the wing-fuselage junction to avoid unnecessary refinement of the discretization on the fuselage side. The body has approximately 45 panels along its length and 24 panels in the circumferential direction. The rear-sting support is also modeled to achieve a better replication of the experimental test conditions. The wake is extended approximately 20 chords behind the wing and its movements are relaxed in order to prevent intersections between wake and body panels during the computations. Moreover, for an accurate prediction of the lift carried out by the fuselage, the shedding lines, prescribed at the wing trailing edges, are necessarily extended downstream along the aft part of the body and the sting.

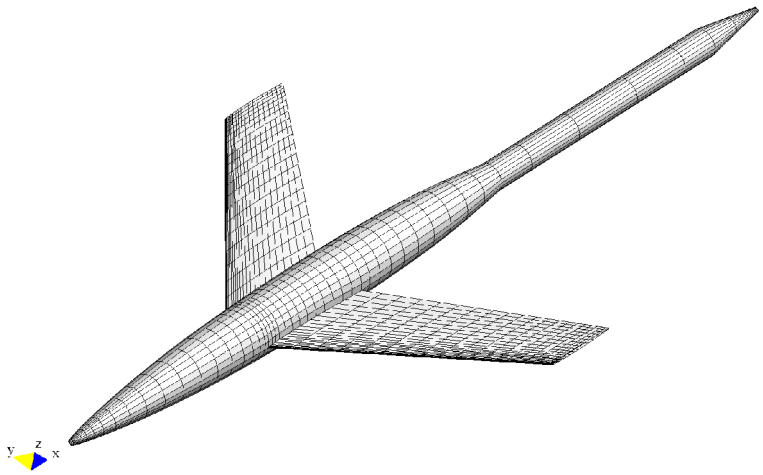

Figure 6. Discretization of the NACA wing-body configuration.

The problem is solved for an angle of attack $\alpha = 4^o$ and the Cp distributions, computed at two spanwise stations $\eta = 2y/b = 0.2$ and $\eta = 0.6$ on the wing, are compared in Figure 7 with experimental measurements reported in [8]. Although those results were obtained for a freestream Mach number $M_\infty = 0.6$, discrepancies with respect to the incompressible computations presented here are not relevant for the adopted angle of attack.

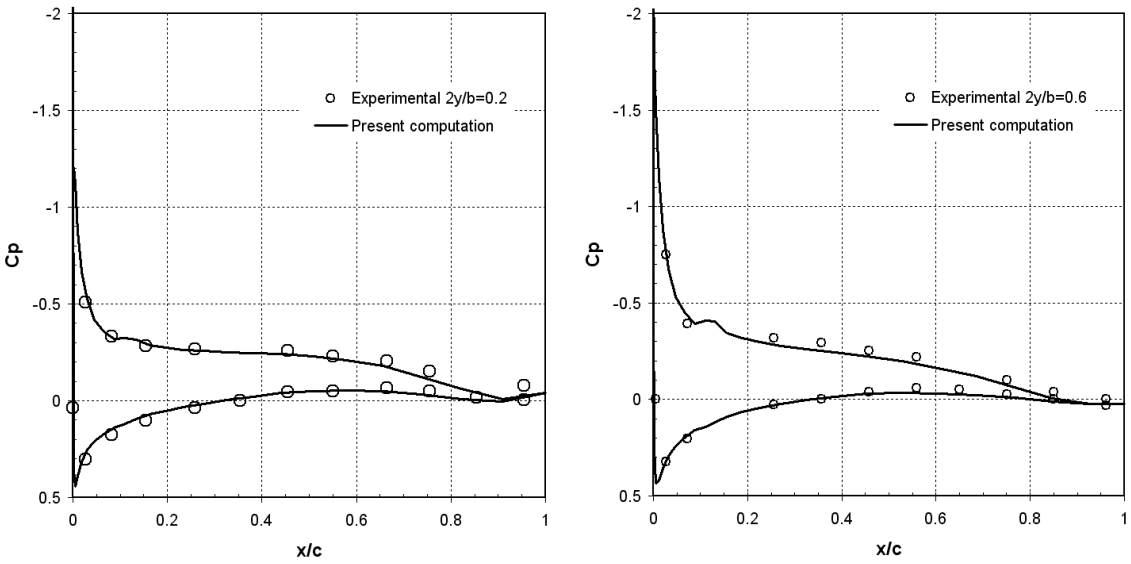

Figure 7. Comparison of computed and experimental Cp distribution along two spanwise wing stations $\eta = 0.2$ and $\eta = 0.6$. NACA wing-body, $\alpha = 4.0^o$.

Figure 8 shows the Cp distribution computed along the fuselage symmetry plane, where a quite satisfactory agreement as well as some minor discrepancies with the experimental results can be seen. Besides, the suction peak seems to be smeared in the numerical solution; however, this effect seems to be caused by the adopted flow model rather than by implementation issues, as a similar behaviour is also observed in [2]. Regarding the numerical

oscillations observed around the body nose, these can be attributed to discretization issues, although possible effects from the body doublicity differentiation should not be ruled out.

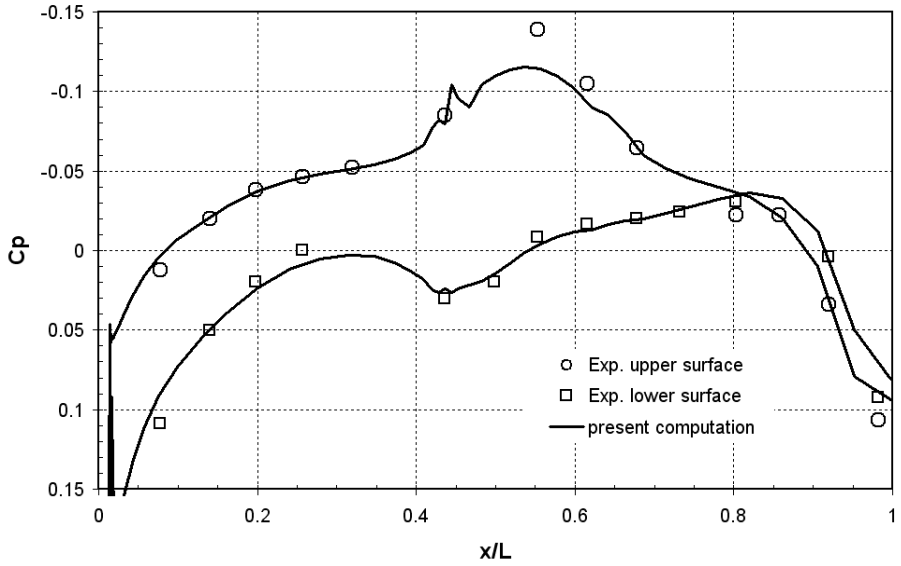

Figure 8. Comparison of computed and experimental Cp distributions along the fuselage symmetry plane. NACA wing-body, $\alpha = 4.0^{o}$.

The normal force and pitching moment coefficients (C_N and C_{My}), computed for angles of attack ranging between -4º and 4º, are plotted in Figure 9 together with force test measurements presented in [8] for $M_\infty = 0.6$ (note that the moment coefficient is computed about the 25-percent position of the wing mean aerodynamic chord). It is possible to observe that our computations have a very good correlation with the experimental results. Finally, the Cp distribution computed over the model is shown in Figure 10.

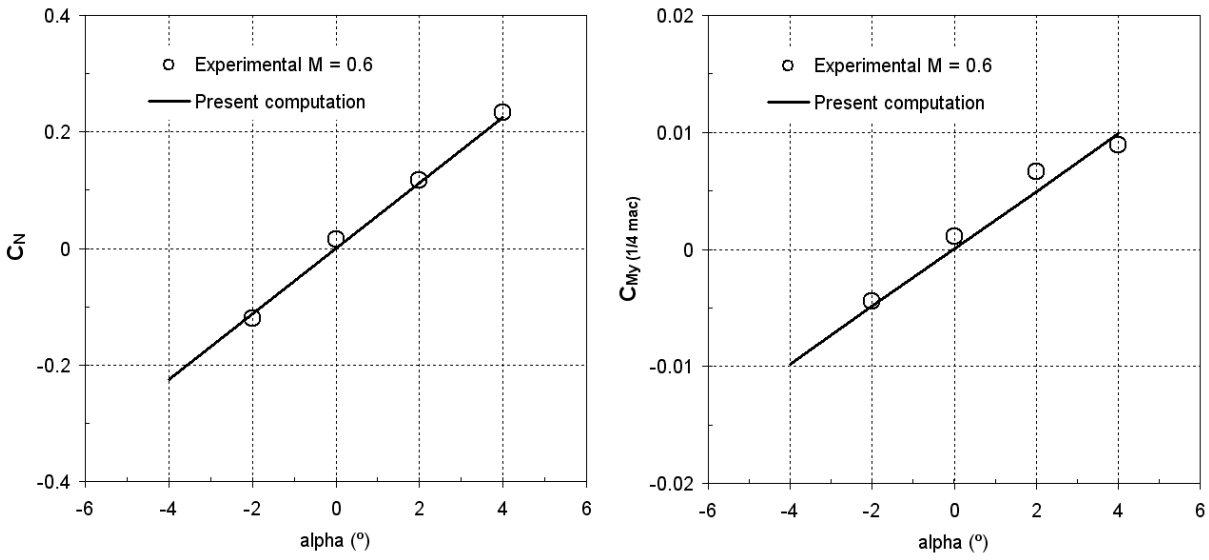

Figure 9. Normal force and pitching moment variation with the angle of attack. NACA wing-body, $\alpha = 4.0^{o}$.

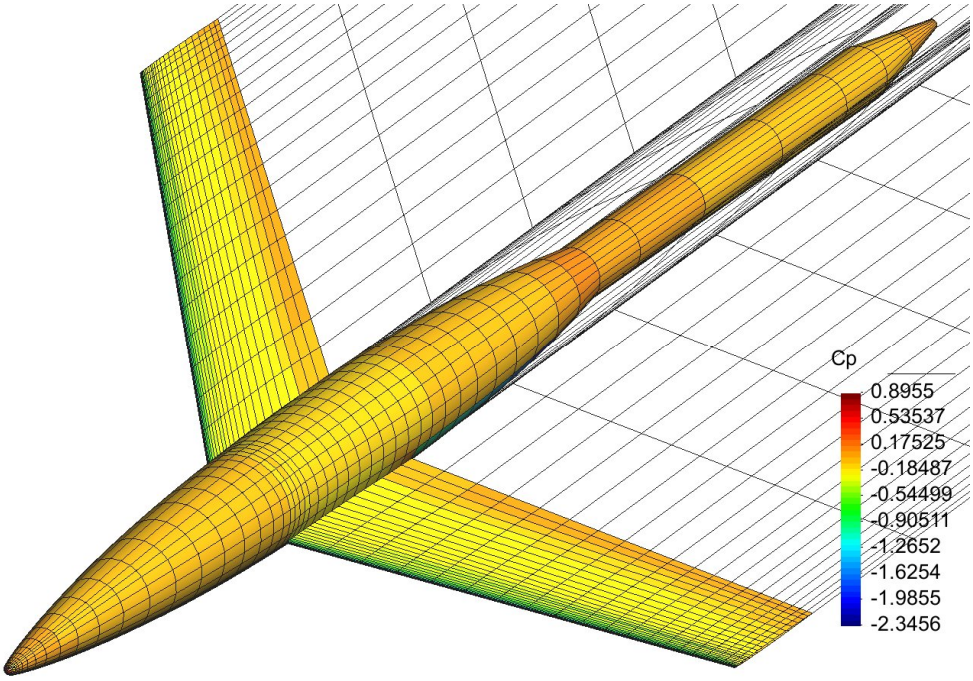

Figure 10: Cp distribution computed on the NACA wing-body, $\alpha = 4.0^{o}$.

6.3 Unsteady analysis of a helicopter rotor in hover flight

The two-blade rotor studied experimentally in [9] is computed in the example presented next. The rotor blades have an aspect ratio A = 6, a taper ratio λ = 1.0 and they do not present neither geometrical twist nor sweep. The airfoil section is a NACA 0012 constant along the span. A rotor radius R = 6, unit chord and a clearance distance between blades equal to 2 chords are adopted in our model. The centre of rotation is located at 25-percent of the chord. Figure 11 shows the discretized rotor geometry composed by a structured distribution of 4000 quadrilateral panels (40 along the span and 25 in the chordwise direction).

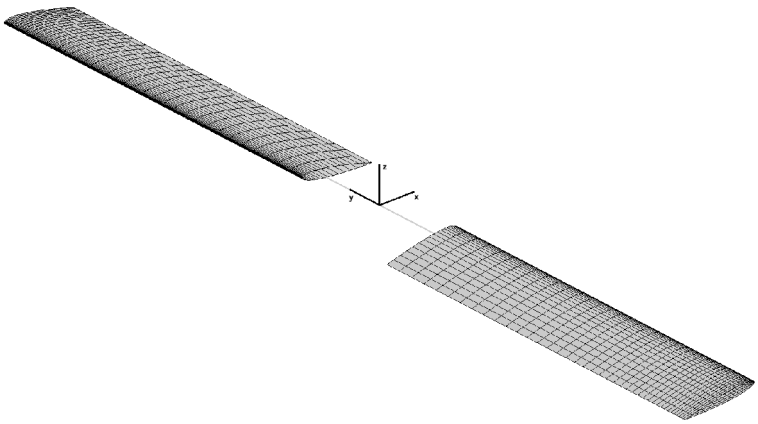

Figure 11. Rotor blades discretization (4000 quadrilateral panels).

Cp distributions are computed on different sections along the blade for collective pitch angles θ_c = 5º and 8º and the results are compared with experimental measurements reported in [9]. In order to minimize the compressible effects that may affect the comparisons, a rotor speed $\Omega_z = 650$ rpm ($M_{tip} \approx 0.225$) is selected according to the lowest angular velocity tested in the study taken as reference. The time increment Δt is selected in such a way that 10 time steps are computed per rotation cycle and the kinematic velocity at each control point (Eq.(5)) is adopted as the reference velocity when computing the coefficient of pressure in Eq. (41). It should be noticed that, as commented in the previous example, the wake movements are limited to avoid body and wake panels intersections, which often lead to numerical misbehaviours during computations.

Figure 12 shows a comparison of Cp distributions at sections r/R = 0.5, 0.8 and 0.96 along the semispan for collective pitch angles θ_c = 5º and 8º. A good correlation can be observed between numerical and experimental results despite the fact that the wake modeling performed in the present case could be further improved. Some snapshots of the problem discretization computed at several instant times during the first rotation cycle are shown in Figure 13 for a collective pitch angle θ_c = 8º. Finally, Figure 14 presents the Cp distribution computed for the same collective pitch angle after several rotation cycles are performed.

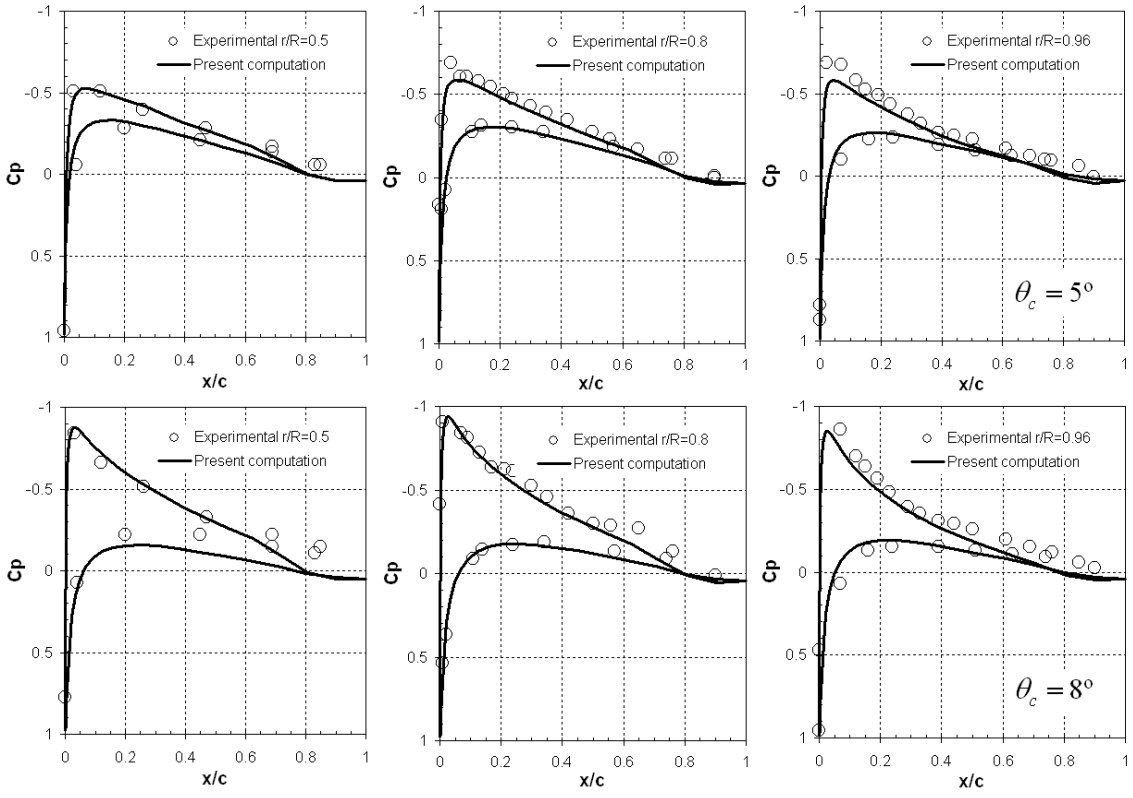

Figure 12. Comparisons of numerical and experimental Cp distributions at different sections along a blade.

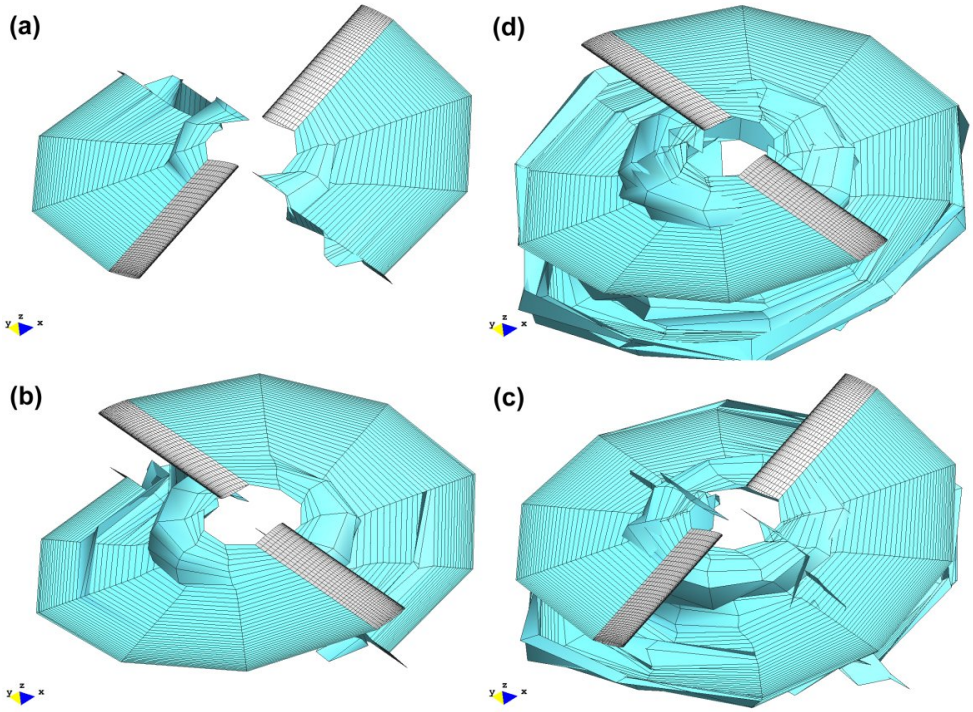

Figure 13. Snapshots of the discrete model computed at different instant times during the first rotation cycle (a→b→c→d). Collective pitch angle $\theta_c = 8^o$.

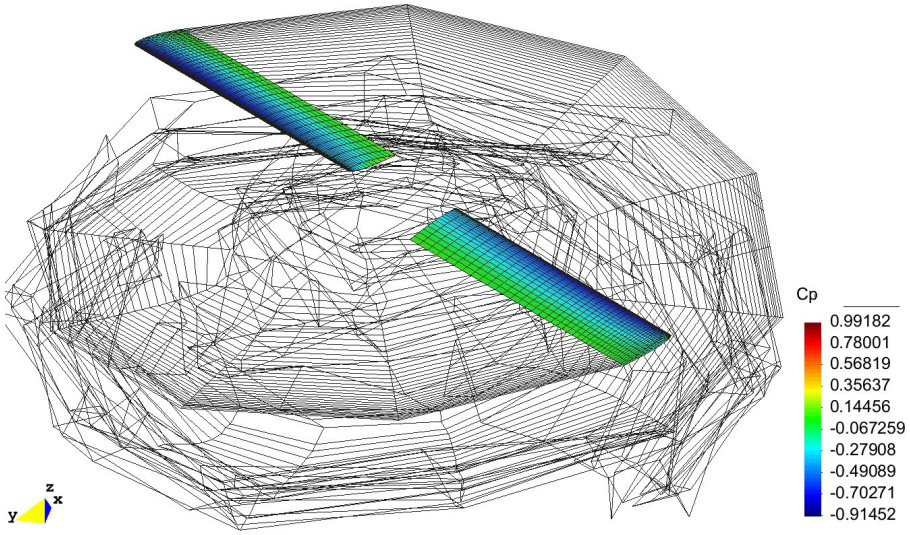

Figure 14. Cp distribution computed over blades for a collective pitch angle $\theta_c = 8^o$.

7. CONCLUSIONS

An unsteady low-order panel method for three-dimensional subsonic analyses has been presented. The focus of this work has been placed on achieving a simulation tool for dealing with arbitrary moving or deforming aerodynamic bodies with minimum discretization efforts

and the lowest computational cost. The three numerical examples presented in this work reinforce the good quality performance of panel techniques reported in the literature.

As a matter of fact, panel techniques reduce drastically the computational cost with respect to other standard volume-based methods. In addition, due to the fact that the most time-consuming computations in panel techniques (such as the evaluation of velocity and potential influence coefficients) can be performed in a completely independent manner, the computational costs can be even more reduced by implementing parallel computing strategies. In spite of the fact that the current computational code is prepared to run in parallel environments using shared memory, it was shown that further efforts are needed in order to obtain a fully parallel code capable of take the most of these advantages. The solution of the aerodynamic influence coefficients system also presents challenging problems from the point of view of parallel execution and storage requirements. As long as storage in concerned, certain alternative techniques, such as matrix lumping, seem to be attractive in order to reduce memory requirements. However, the feasibility of implementing these techniques in the present context should be further investigated.

REFERENCES

[1] Katz, J. and Plotkin, A. Low-Speed aerodynamics. From wing theory to panel methods., McGraw-Hill, 1991.

[2] Ashby, D. L. Potential flow theory and operation guide for the panel code PMARC_14. *NASA TM-1999-209582,* 1999.

[3] Magnus, A. E. and Epton, M. A. PAN AIR - A computer program for predicting subsonic or supersonic linear potential flows about arbitrary configurations using a higer order panel method. Volume I. Theory document (version 1.0). *NASA CR 3251,* 1980.

[4] Erickson, L. Panel methods. An introduction. *NASA Technical Paper NASA-TP-2995,* 1990.

[5] Maskew, B. Program VSAERO theory document. A computer program for calculating nonlinear aerodynamic characteristics of arbitrary configurations. *NASA Report 4023,* 1987.

[6] Katz, J. and Maskew, B. Unsteady low-speed aerodynamic model for complete aircraft configurations. *AIAA-86-2180,* 1986.

[7] Preidikman, S. Numerical simulations of interactions among aerodynamics, structural dynamics, and control systems. *Ph.D. Thesis, Virginia Polytechnich Institute and State University,* 1998.

[8] Loving, D. and Estabrooks, B. Transonic-wing investigation in the Langley 8-foot high-speed tunnel at high subsonic Mach numbers and at a Mach number of 1.2. Analysis of pressure distribution of wing-fuselage configuration having a wing of 45º sweepback, aspect ratio 4, taper ratio 0.6, and NACA 65A006 airfoil section. *National Advisory Committee for Aeronautics. Research Memorandum NACA RM L51F07,* 1951.

[9] Caradonna, F. X. and Tung, C. Experimental and analytical studies of a model helicopter rotor in hover. *NASA Technical Memorandum NASA-TM-81232,* 1981.